

Cite this: *Nanoscale*, 2017, **9**, 16329

## Thermal and electronic transport characteristics of highly stretchable graphene kirigami†

Bohayra Mortazavi,<sup>‡</sup> Aurélien Lherbier,<sup>‡</sup> Zheyong Fan,<sup>‡</sup> Ari Harju,<sup>d</sup> Timon Rabczuk<sup>e</sup> and Jean-Christophe Charlier<sup>b</sup>

For centuries, cutting and folding papers with special patterns have been used to build beautiful, flexible and complex three-dimensional structures. Inspired by the old idea of kirigami (paper cutting), and the outstanding properties of graphene, recently graphene kirigami structures were fabricated to enhance the stretchability of graphene. However, the possibility of further tuning the electronic and thermal transport along the 2D kirigami structures has remained original to investigate. We therefore performed extensive atomistic simulations to explore the electronic, heat and load transfer along various graphene kirigami structures. The mechanical response and thermal transport were explored using classical molecular dynamics simulations. We then used a real-space Kubo–Greenwood formalism to investigate the charge transport characteristics in graphene kirigami. Our results reveal that graphene kirigami structures present highly anisotropic thermal and electrical transport. Interestingly, we show the possibility of tuning the thermal conductivity of graphene by four orders of magnitude. Moreover, we discuss the engineering of kirigami patterns to further enhance their stretchability by more than 10 times as compared with pristine graphene. Our study not only provides a general understanding concerning the engineering of electronic, thermal and mechanical response of graphene, but more importantly can also be useful to guide future studies with respect to the synthesis of other 2D material kirigami structures, to reach highly flexible and stretchable nanostructures with finely tunable electronic and thermal properties.

Received 18th July 2017,  
Accepted 20th September 2017

DOI: 10.1039/c7nr05231f

rs.c.li/nanoscale

### 1. Introduction

The two-dimensional form of  $sp^2$  carbon atoms, so called graphene,<sup>1–3</sup> is widely considered as a wonder material owing to its exceptional mechanical,<sup>4</sup> thermal<sup>5</sup> and electronic<sup>3</sup> properties. Graphene in its single-layer and free-standing form exhibits a unique combination of ultra-high mechanical and thermal conduction properties, which include a Young's modulus of about 1000 GPa, an intrinsic strength of about 130 GPa<sup>4</sup> and a thermal conductivity of around 4000 W m<sup>-1</sup> K<sup>-1</sup>,<sup>6</sup> outperforming all known materials. These unique properties

of graphene offer it as a promising candidate for a wide variety of applications such as simultaneously enhancing the thermal, electronic and mechanical properties of polymer nanocomposites, stretchable nanoelectronics, nanosensors, nano-resonators and nanoelectromechanical systems (NEMS). The great achievements of graphene promoted the successful synthesis of other high-quality 2D materials like hexagonal boron nitride,<sup>7</sup> silicene,<sup>8,9</sup> phosphorene,<sup>10,11</sup> borophene,<sup>12</sup> germanene,<sup>13</sup> and transition metal dichalcogenides (TMDs) like MoS<sub>2</sub>.<sup>14</sup> An interesting fact about graphene lies in its unique ability to present largely tunable<sup>15–17</sup> and in some cases contrasting properties through mechanical straining,<sup>18–22</sup> defect engineering<sup>23–26</sup> or chemical doping.<sup>27–32</sup>

Apart from the latest scientific advances during the past decade, origami is an old Chinese and Japanese art with a simple idea of transforming a flat paper into a complex and elaborated three-dimensional structure through folding and sculpting techniques. This idea is well-explained by the Japanese word origami, where “ori” means “folding” and “kami” means “paper”. Kirigami (“kiru” means cutting) is another variation of origami which includes solely the cutting of the paper, and therefore it is different from origami which is achieved only by paper folding. As mentioned earlier, graphene presents exceptionally high mechanical strength and

<sup>a</sup>Institute of Structural Mechanics, Bauhaus-Universität Weimar, Marienstr. 15, D-99423 Weimar, Germany. E-mail: bohayra.mortazavi@gmail.com

<sup>b</sup>Université catholique de Louvain, Institute of Condensed Matter and Nanosciences, Chemin des étoiles 8, 1348 Louvain-la-Neuve, Belgium.

E-mail: aurelien.lherbier@uclouvain.be

<sup>c</sup>School of Mathematics and Physics, Bohai University, Jinzhou, China

<sup>d</sup>COMP Centre of Excellence, Department of Applied Physics, Aalto University, Helsinki, Finland. E-mail: zheyong.fan@aalto.fi

<sup>e</sup>College of Civil Engineering, Department of Geotechnical Engineering, Tongji University, Shanghai, China

†Electronic supplementary information (ESI) available. See DOI: 10.1039/c7nr05231f

‡These three first co-authors contributed equally.

stiffness, but the stretchability of graphene is limited because of its brittle failure mechanism.<sup>4,33</sup> For many applications such as those related to flexible nanoelectronics, the building blocks are requested to present a ductile mechanical response and the brittle nature of graphene acts as a negative factor. Therefore, engineering of the graphene structure to enhance its ductility and more generally to provide a tunable mechanical response can provide more opportunities for graphene applications. To address this issue and inspired by the ancient idea of kirigami, an exciting experimental advance has been recently achieved with respect to the fabrication of graphene kirigami, through employing the lithography technique.<sup>34,35</sup> Experimental results confirmed the considerable enhancement in the stretchability and bending stiffness of graphene through applying the kirigami approach.<sup>34</sup> This experimental advance consequently raised the importance of theoretical investigations to provide more in-depth physical insight. Using classical molecular dynamics simulations, both mechanical<sup>36,37</sup> and thermal conductivities<sup>38</sup> of graphene kirigami were studied. In these investigations,<sup>36,38</sup> similar to the experimental set-up,<sup>34</sup> graphene films with only few linear cuts were investigated. However, in another amazing experimental study,<sup>39</sup> the kirigami approach with periodic and curved-cuts was employed for the engineering of elasticity in polymer nanocomposites. This recent experimental study on the polymer nanocomposite kirigami<sup>39</sup> films consequently highlights the possibility of the fabrication of graphene kirigami structures with networks of curved cuts rather than a few straight cuts (as was proposed in the earlier investigation<sup>34</sup>). Because of the complexities of such experimental set-ups, theoretical studies can be considered as promising alternatives to shed light on the properties of these structures. To the best of our knowledge, mechanical, thermal and electronic transport properties of graphene kirigami nanomembranes with periodic and curved cutting patterns have not been studied. This study therefore aims to explore the transport properties of the graphene kirigami with different cutting patterns using large scale atomistic simulations.

## II. Models and methods

### A. Graphene kirigami structural design

The graphene kirigami structures explored in this study were constructed by considering periodic boundary conditions such that they represent graphene films with repeating cuts.<sup>39</sup> In order to describe our modeling strategy, as shown in Fig. 1, a sample of the constructed molecular model of graphene kirigami is illustrated, along with the geometric parameters. The length of the cuts ( $l_c$ ) is the first parameter that describes the graphene kirigami. The width of the cuts is accordingly changed to adjust the volume fraction of the materials removed from the graphene. In this work, we considered curved cuts which are defined by the curvature angle ( $\theta$  in Fig. 1). In this way, the curvature angles of 0 and 180 degrees

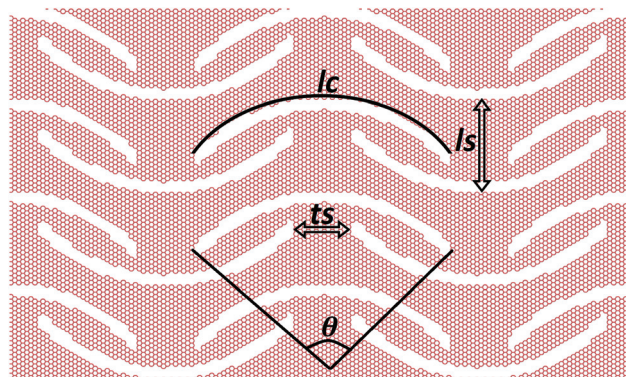


Fig. 1 Atomistic and periodic structure of graphene kirigami, to illustrate the key geometric parameters: the curvature angle ( $\theta$ ), and the longitudinal and transverse spacing distances ( $l_s$  and  $t_s$ ).

represent straight and half-circular cuts, respectively. The longitudinal ( $l_s$  in Fig. 1) and transverse ( $t_s$  in Fig. 1) spacing distances between two adjacent cuts are two other key parameters used to characterize the graphene kirigami structures. In our modeling, the cut length was considered as the main factor, which directly determines the system scale. By scaling the cut length, other parameters were also scaled with exactly the same ratio to keep the overall geometry of graphene kirigami consistent.

### B. Stretchability and thermal transport properties

We employed classical molecular dynamics (MD) simulations to evaluate the mechanical and thermal transport properties of graphene kirigami structures. The atomic interaction between carbon atoms was modelled using the Tersoff potential,<sup>40,41</sup> optimized by Lindsay and Broido.<sup>42</sup> Among the different possibilities for the modeling of graphene structures, the optimized Tersoff potential is highly efficient and can be used to simulate large scale systems. More importantly, it gives reasonable predictions of both thermal conductivity and mechanical properties of pristine graphene as compared with experimental results.<sup>43–45</sup> In our classical MD simulations, we applied periodic boundary conditions along the  $x$ - $y$  planar directions. In the evaluation of the mechanical response and thermal conductivity of graphene kirigami nanomembranes, we assumed a thickness of 3.35 Å, the same as that of pristine graphene. We employed the equilibrium molecular dynamics (EMD) method to calculate the thermal conductivity of the graphene kirigami structures, using GPUMD,<sup>46</sup> an efficient MD code fully implemented on graphics processing units, to compute the thermal conductivity of large scale graphene kirigami structures. We calculated the heat flux vector with the appropriate form for many-body potentials as described in ref. 45:

$$\mathbf{J} = \sum_i \sum_{j \neq i} (\mathbf{r}_j - \mathbf{r}_i) \left( \frac{\partial U_j}{\partial \mathbf{r}_{ji}} \cdot \mathbf{v}_i \right), \quad (1)$$

where  $\mathbf{v}_i$  is the velocity of atom  $i$ ,  $\mathbf{r}_i$  is the position vector of atom  $i$ ,  $\mathbf{r}_{ji}$  is the position vector from atoms  $j$  to  $i$ , and  $U_j$  is the potential energy associated with atom  $j$ . The thermal conductivity tensor can be acquired based on the Green–Kubo formula:

$$\kappa_{\alpha\beta} = \frac{1}{Vk_{\text{B}}T^2} \int_0^\infty \langle \mathbf{J}_\alpha(0)\mathbf{J}_\beta(t) \rangle dt, \quad (2)$$

where  $k_{\text{B}}$  is Boltzmann's constant,  $T$  is the simulation temperature, and  $V$  is the total volume of the system. Thermal transport in graphene kirigami nanomembranes is anisotropic, and the thermal conductivities of a given sample were calculated in both the longitudinal and transverse directions. We note that when using the EMD method, accurately predicting the converged thermal conductivity requires performing many independent simulations and averaging them.<sup>47</sup> We remind that because of the use of an inaccurate heat-flux formula for many-body interactions, the LAMMPS<sup>48</sup> implementation of the EMD method significantly underestimates the thermal conductivity of graphene.<sup>45</sup>

Then, we evaluated the mechanical response of graphene kirigami structures by performing uniaxial tensile tests at room temperatures. In this case, we used LAMMPS,<sup>48</sup> a free and open-source package. As was discussed in a recent study,<sup>44</sup> we modified the inner cutoff of the Tersoff potential from 0.18 nm to 0.20 nm, which was found to accurately reproduce the experimental results for the mechanical properties of pristine graphene. The time increment of these simulations was set as 0.2 fs. Before applying the loading conditions, all structures were relaxed and equilibrated using the Nosé–Hoover barostat and thermostat method (NPT ensemble). For the loading condition, we increased the periodic size of the simulation box along the loading direction at every time step and at an engineering strain rate of  $5 \times 10^8 \text{ s}^{-1}$ . Simultaneously, in order to ensure the uniaxial stress condition, the stress along the transverse direction was controlled using the NPT ensemble.<sup>44</sup> To report the stress–strain relations, we calculated the virial stresses every 2 fs and then averaged them over every 20 ps intervals.

### C. Electronic transport properties

The electronic and transport calculations, including electronic densities of states (DOS) per unit of surface ( $\rho(E) = \text{Tr}[\delta(E - \hat{H})/S]$ ) and Kubo–Greenwood conductivities ( $\sigma(E, L)$ ), rely on a well-established real-space Kubo–Greenwood method.<sup>24,49–55</sup> The electronic framework is based on a tight-binding (TB) Hamiltonian described by a  $\pi$ - $\pi^*$  TB orthogonal model (one orbital per carbon atom) with interactions up to the third nearest neighbors (hopping terms are obtained as  $\gamma(d) = \gamma_0 e^{-3.37(d/d_{\text{CC}} - 1)}$ , with  $\gamma_0 = -2.8 \text{ eV}$  and  $d_{\text{CC}} = 1.42 \text{ \AA}$ ).<sup>56,57</sup> The Kubo–Greenwood approach combines a Lanczos recursion scheme to obtain spectral quantities such as the DOS<sup>58</sup> and a Chebyshev polynomial expansion method to compute the time-dependent electronic diffusivity ( $D(t)$ ) through the evaluation of the time evolution operator  $\hat{U}(t) = \prod_{n=0}^{N-1} \exp(i\hat{H}\Delta t/\hbar)$ ,

with  $\Delta t$  as the chosen time step. The total diffusivity is expressed as  $D = D_x + D_y$  with  $D_x(E, t) = \frac{\partial \Delta X^2(E, t)}{\partial t}$  and  $\Delta X^2(E, t) = \text{Tr}[\delta(E - \hat{H})|\hat{X}(t) - \hat{X}(0)|^2] / \text{Tr}[\delta(E - \hat{H})]$ . Traces are evaluated by averaging on eight random phase wave packets ( $N_{\text{rppwp}} = 8$ ) on large enough systems. More explicitly, for a given operator  $\hat{A}$ , one has

$$\text{Tr}[\hat{A}] = \sum_{i=1}^{N_{\text{orb}}} \langle \phi_i | \hat{A} | \phi_i \rangle \simeq \frac{N_{\text{orb}}}{N_{\text{rppwp}}} \sum_{j=1}^{N_{\text{rppwp}}} \langle \phi_j | \hat{A} | \phi_j \rangle, \text{ where } |\phi_i\rangle \text{ is the}$$

$i^{\text{th}}$  orbital over  $N_{\text{orb}}$  orbitals and  $|\phi_j\rangle = \frac{1}{\sqrt{N_{\text{orb}}}} \sum_{i=1}^{N_{\text{orb}}} |\phi_i\rangle e^{i\theta_i^j}$  is a

random phase wave packet ( $\theta_i^j$  is a random angle). At short time,  $D_{x,y}(t)$  is linear in time with the slope being the average square velocity  $v_{x,y}^2(t=0)$ . In the following, the considered graphene kirigami structures are constructed by repeating periodically a rectangular unit cell whose dimensions increase with the cut length ( $l_c = 10, 20, 40, 80,$  and  $160 \text{ nm}$ ). Because of this perfect periodicity, *i.e.* without the introduction of any stochastic disorder, the long time behavior of the diffusivity  $D(t)$  should be in the ballistic regime, *i.e.* a linear increase in time with the slope being  $v_{x,y}^2(t=\infty)$ . These two ballistic regimes and their associated velocities ( $v^2(t=0)$  and  $v^2(t=\infty)$ ) are in principle different. The short time velocity corresponds to the dynamics of charge at a small scale, *i.e.* a graphene honeycomb lattice, while the long time velocity corresponds to the propagation associated with the Bloch states of the periodic kirigami structure. However, to observe this second ballistic signature, the simulated time propagation has to be very long, especially for the large cuts, such that the periodicity effects at a large scale become sufficiently significant. Actually, because of computing limitations, this second ballistic regime is not always reached. In between these two ballistic regimes, an intermediate regime should be observed and may include (pseudo) diffusive and/or localization regimes, that is a (slow increase) saturation of  $D(t)$  and/or a decrease of  $D(t)$ , respectively. These regimes correspond to the fact that at the intermediate length scale, the electron wave propagation encounters scattering related to the presence of cuts and interferences related to these multiple scattering events. A similar transient phenomenon was observed in a previous study on carbon nanotubes doped periodically with nitrogen atoms.<sup>59</sup> The determination of mean elastic scattering times and paths ( $\tau$  and  $l_e$ , respectively) is not easily practicable in systems containing two periodic patterns, which are in the present case the honeycomb and the kirigami lattices, because of the complex dynamics of charge carriers. Instead of characterizing the systems with the evaluation of  $\tau$  and  $l_e$ , it is preferable to describe the transport with a well-defined quantity which is the Kubo–Greenwood length-dependent conductivity ( $\sigma(E, L)$ ). Since the kirigami structures present anisotropy, it is also important to consider independently the two longitudinal components of the conductivity tensor ( $\sigma_{xx}(E, L)$  and  $\sigma_{yy}(E, L)$ ). The former reads  $\sigma_{xx}(E, L) = \frac{1}{2} e^2 \rho(E) \frac{\partial \Delta X^2(E, t)}{\partial t} \Big|_{t=t_L} \text{ with } L=2\sqrt{\Delta X^2(E, t_L)}$ .

### III. Results and discussion

#### A. Thermal transport

We first study heat transport along the graphene kirigami films. Since in the EMD method periodic boundary conditions are applied and the systems are at equilibrium (no external heat-flux or temperature boundary conditions are applied), this method is much less sensitive to the finite-size effects as compared to the non-equilibrium molecular dynamics (NEMD) method<sup>47</sup> or the approach-to-equilibrium molecular dynamics (AEMD) method.<sup>60</sup> As discussed in a recent study,<sup>61</sup> the EMD method predicts a thermal conductivity of  $2900 \pm 100 \text{ W m}^{-1} \text{ K}^{-1}$  for pristine graphene at room temperature. In this case, a relatively small simulation cell size (with  $\sim 10^4$  atoms) is sufficient to eliminate the finite-size effects.<sup>45</sup> However, using the NEMD or the AEMD method, the thermal conductivity of graphene keeps increasing by increasing the sheet length and the thermal conductivity was found to not fully converge even up to 0.1 mm.<sup>62</sup> Interestingly, for the graphene kirigami structures with periodic cutting patterns, the EMD method can be used to evaluate the full thermal conductivity tensor by constructing a single sample of moderate size. However, using the NEMD or AEMD method the length dependency of the predicted thermal conductivity values should be assessed, which demands high computational costs associated with the modeling of several large samples, each with different lengths. In Fig. 2, typical EMD results for the calculated thermal conductivity along the longitudinal and transverse directions are presented as a function of correlation time, for graphene kirigami samples with cut lengths of 10 nm and 160 nm at room temperature. In this case, the volume fraction of the cuts is 20% and samples with curvature angles of  $0^\circ$ ,  $90^\circ$  and  $180^\circ$  for the cuts are considered. For samples with a larger cut length, the

predicted thermal conductivity values are considerably higher (see Fig. 2). As expected, along the longitudinal direction, since the cut sections interfere directly with the phonon transport, the thermal conductivity is much more suppressed as compared with the transverse direction in which the cuts are basically parallel to the heat transfer direction (see the ESI†). Moreover, based on our results along the longitudinal direction of the sample with small cut lengths, the effects of cut curvature angle on the thermal conductivity are small. The running thermal conductivity in this direction also exhibits a local peak at small correlation time, which is a sign of pseudo diffusive transport and localization caused by the combined honeycomb and kirigami lattices, as in the case of electron transport (see the Models and method section). For heat transfer along the transverse direction, by increasing the curvature angle the thermal conductivity decreases significantly, which can be related to the increased obstruction in the direction of phonon transport.

In a recent investigation,<sup>61</sup> a decomposition of the thermal conductivity of 2D materials into contributions from in-plane and out-of-plane phonons was introduced. For pristine graphene, the out-of-plane and in-plane components of the thermal conductivity were predicted to be  $2050 \text{ W m}^{-1} \text{ K}^{-1}$  and  $850 \text{ W m}^{-1} \text{ K}^{-1}$ , respectively. To gain more insight concerning the underlying mechanisms responsible for the suppression of thermal conductivity along the graphene kirigami structures, the calculated out-of-plane and in-plane thermal conductivity components are compared in Fig. 3 along the transverse direction of graphene kirigami networks with a 20% concentration of 160 nm long cuts. In contrast to the thermal transport in the pristine graphene, the in-plane phonons contribute more to the thermal conductivity than the out-of-plane phonons in graphene kirigami structures. For example, in the case of  $0^\circ$  degree cuts, the in-plane and out-of-plane thermal conductivity components are about  $400 \text{ W m}^{-1} \text{ K}^{-1}$  and  $300 \text{ W m}^{-1} \text{ K}^{-1}$ , respectively, which are about 1/2 and 1/7 of the corresponding values in pristine graphene. This clearly demonstrates that the

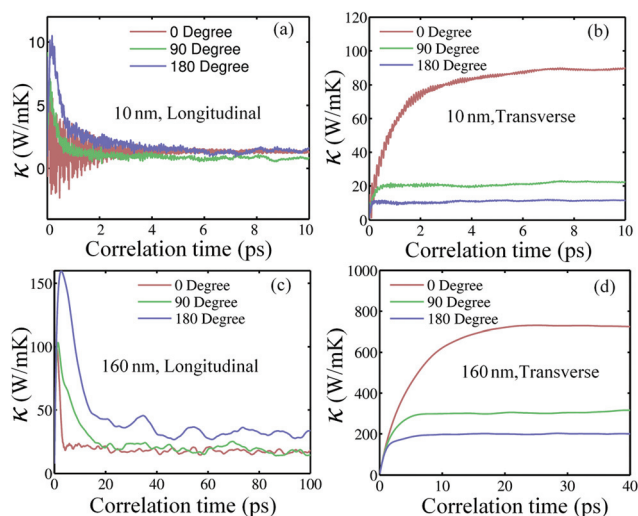


**Fig. 2** Thermal conductivities of graphene kirigami at room temperature along the longitudinal (a, c) and transverse (b, d) directions as a function of correlation time, for samples with cut lengths of 10 nm (a, b) and 160 nm (c, d) and curvature angles of  $0^\circ$ ,  $90^\circ$  and  $180^\circ$  degrees.

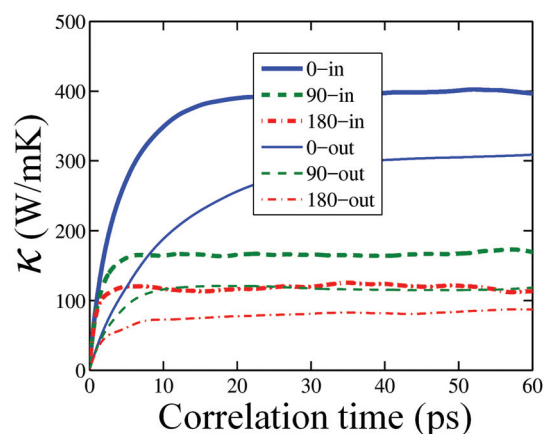


**Fig. 3** Thermal conductivity components contributed by out-of-plane (out) and in-plane (in) phonons in the transverse direction for graphene kirigami structures with a 20% concentration of 160 nm long cuts.

suppression of out-of-plane phonons plays the major role in the decline of the thermal transport along graphene kirigami films. This is similar to the case of supported graphene where the out-of-plane phonons are strongly suppressed by a substrate.<sup>63</sup>

For the kirigami systems, because of the cut patterns, the heat flux flows through a complicated path which consequently affects the thermal conductivity. For these systems at the atomic scale, the thermal transport is however dominated by the phonon-cut scattering effects. Nevertheless, by increasing the cut length and approaching the mean-free-path of graphene, the effect of phonon-cut scattering on the suppression of thermal transport decreases and by further increasing of the length scale this effect vanishes and the thermal conductivity converges. In this way, for the kirigami structures with the large cuts at the microscale, the effective thermal conductivity approaches the diffusive heat transfer, which can be studied on the basis of a continuum system that neglects the phonon-cut scattering rates. Based on this preliminary discussion, the main reason that contributes to the length effect in the thermal transport of graphene kirigami structures is the phonon-cut scattering. Nonetheless, from the continuum point of view, the effective thermal conductivity along the kirigami structures is not trivial and to the best of our knowledge no analytical function exists to describe such a diffusive process. We therefore employed finite element (FE) modeling to evaluate the effective thermal conductivity of kirigami films at the diffusive limit. In this study, the FE simulations were carried out using the ABAQUS/Standard package. As for the loading conditions, we applied positive (inward) and negative (outward) heat-fluxes on the two opposite surfaces along the direction in order to investigate the thermal conductivity. Since the thermal transport is investigated along the periodic structures, on the boundary edges perpendicular to the heat-transfer direction, the temperatures of every two opposite nodes should be equal which can be achieved by applying periodic boundary conditions in the FE modeling. We calculated the temperature gradient along the heat transfer direction which was then accordingly used to compute the effective thermal conductivity on the basis of Fourier's law.<sup>64</sup>

To account for atomistic effects which are related to the phonon-cut scattering rates, one can assume these cuts as resistors that scatter the phonons. In such a way, the effective thermal conductivity of kirigami films can be approximated by considering a series of line conductors (representing the graphene pristine lattices) that are connected by thermal resistors (representing the cuts). As discussed in an earlier study for the modeling of heat transfer in polycrystalline graphene,<sup>64</sup> the effective thermal conductivity of such a system can be represented based on the first order rational curve. In order to simulate the effective thermal conductivity of graphene kirigami structures with larger cut lengths, we therefore extrapolated the EMD results for small cut lengths using the first order rational curve. In these cases, we considered that the thermal conductivity of the kirigami films with infinite cut lengths is equal to that based on our FE diffusive modeling. In

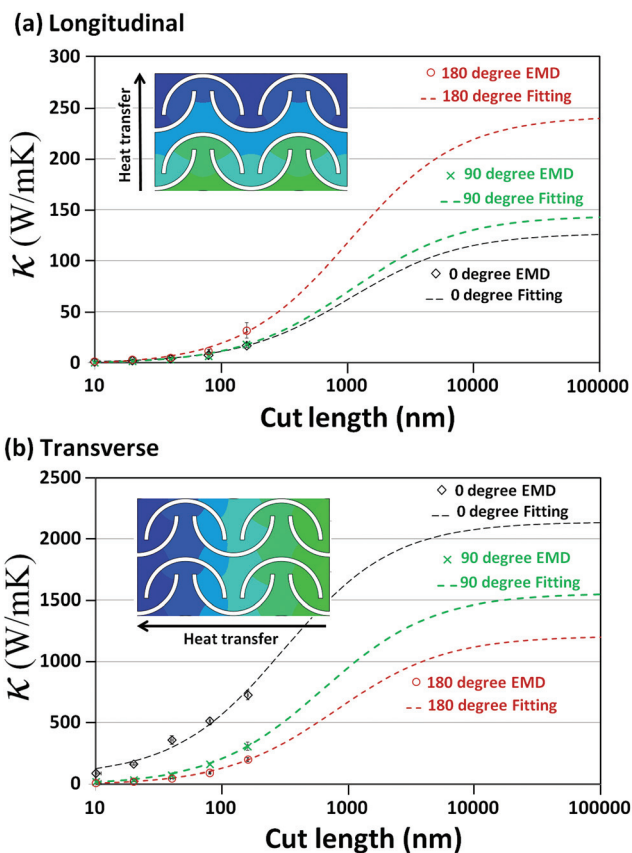


Fig. 4 Effective thermal conductivities of graphene kirigami structures at the room temperature as a function of cut length along (a) the longitudinal and (b) transverse directions. The points and dashed lines represent the EMD results and extrapolation curves, respectively. The insets illustrate the finite element modeling results for the temperature distributions of systems in the diffusive regime.

Fig. 4, the calculated effective thermal conductivities of graphene kirigami structures by the EMD method as a function of cut length along the longitudinal and transverse directions are illustrated. Interestingly, the devised extrapolation technique can reproduce fairly well the trends acquired by the fully atomistic EMD modeling. This result suggests that the combination of EMD and FE modeling can be used as an efficient approach to estimate and engineer the effective thermal conductivity of graphene kirigami structures for different cut lengths and curvature angles as well. We should also note that the thermal conductivity of graphene can be engineered by at least three orders of magnitude based on the kirigami approach. We remind that the thermal conductivity of highly defective graphene, so called amorphized graphene, was found to be around two orders of magnitude smaller than that of pristine graphene.<sup>44</sup> Moreover, chemical doping was predicted to reduce the thermal conductivity of graphene by around an order of magnitude.<sup>65</sup> This short comparison clearly highlights the fact that the fabrication of graphene kirigami networks can be considered as a very effective method to tune the thermal transport properties in graphene-based nano-

structures. It should be noted that in this study we did not consider the effect of loading strain on the thermal transport of kirigami structures. Nonetheless, recent theoretical studies<sup>66–69</sup> have confirmed that by applying the strain the thermal conductivity of pristine 2D materials may increase substantially. Therefore, exploring the strain-tunability of thermal transport in the kirigami structures can be an attractive topic for future studies.

## B. Stretchability

According to our acquired stress–strain curve for pristine graphene at room temperature (Fig. 5 inset), the elastic modulus and tensile strength are predicted to be  $960 \pm 10$  GPa and  $132 \pm 2$  GPa, respectively. These predictions are in excellent agreement with the experimental results of  $1000 \pm 100$  GPa and  $130 \pm 10$  GPa for the elastic modulus and tensile strength of pristine graphene, respectively, reported by Lee *et al.*<sup>4</sup> We next shift our attention to explore the mechanical response and stretchability of the graphene kirigami structures. As observed for thermal transport, due to the phonon-cut scattering effects the cut length plays the major role. In contrast, for the stretchability of the graphene kirigami, the deflection of the sheets and stress-concentration originated from the cuts are the main factors that should be taken into account. To investigate the effect of cut length on the stress–strain response, we considered different structures with linear cuts and with different cut lengths and the acquired results are shown in Fig. 5. As compared with pristine graphene (Fig. 5 inset), the stress–strain responses of graphene kirigami present different patterns. In pristine graphene, the applied strain directly results in increasing of the carbon atom bond length and therefore the stress value increases considerably by increasing the strain. In contrast, for the considered graphene kirigami structures, up to high strain levels of  $\sim 1$ , the stress value increases only slightly and remains very low which indicates that the structure

elongates by deflection rather than the stretching of the carbon bonds. After the strain level of  $\sim 1$ , the stress values start to increase but in a smooth manner, which implies that the deformation is yet achieved by the deflection but bond elongation is also happening. The remarkable deflection of graphene kirigami upon stretching can be partially explained by the standard deviation of the  $z$ -coordinates ( $S_z$ ).<sup>70</sup>  $S_z$  was calculated using

$$S_z = \sqrt{\frac{\sum_{i=1}^N (z_i - z_0)^2}{N}},$$

where  $z_i$  is the  $z$ -coordinate of the  $i$ -th

atom,  $z_0$  is the averaged  $z$ -coordinate of all atoms and  $N$  is the total number of atoms. In Fig. 5, we also plotted the computed  $S_z$  for a graphene kirigami with a cut length of 40 nm. As is clear, up to the strain level of  $\sim 1$ , the  $S_z$  keeps increasing, which further confirms the considerable out-of-plane deflection of the structure. However, after the strain level of  $\sim 1$ , a plateau is observable which means that the out-of-plane deflection of the structure becomes substantially limited.

For the considered structures, at strain levels higher than  $\sim 1.6$ , the stress values sharply increase which reveals that the deflection of the sheets contributes less to the stretching and that the stretching is achieved more by the bond elongation. Because of the limited stretchability of the carbon atom bond, this step is limited and shortly after the structure reaches its failure point. At this stage, the stress concentration existing around the cut corners results in the local and instantaneous bond breakages, thus causing instabilities and accordingly variations in the stress values. Around the cut corners, the bond breakages extend gradually and the rupture finally occurs when the two parts of the kirigami become completely detached by the crack coalescence. Since we considered the thermal effects by conducting the simulation at room temperature, the bond breakages present a stochastic nature and therefore a sample presents different stress–strain relations around the failure point by performing independent simulations with different initial velocities. In accordance with earlier observations,<sup>36</sup> our results shown in Fig. 5 also confirm that the stretchability of the graphene kirigami is convincingly independent of the cut length. This is an important finding and illustrates that the classical MD simulations can be considered as a promising approach for the design of graphene kirigami structures with optimized performance. It is worth noting that in this case, the finite element modeling is highly complicated mainly because of the existing severe out-of plane deflections and also stress-concentrations (that may cause singularity in the stress field). As is clear for different samples, the variations for the maximum tensile strength are more considerable than the rupture strain of the graphene kirigami films. From an engineering point of view, the main goal to fabricate the graphene kirigami is to enhance the stretchability such that the values of the tensile strength are not critical. For the rest of our investigation, we considered the cut length of 40 nm and for each case we performed 4 independent simulations to provide the error-bars in our results.

In Fig. 6, the deformation process of two different graphene kirigami structures is depicted. The deformation is highly sym-

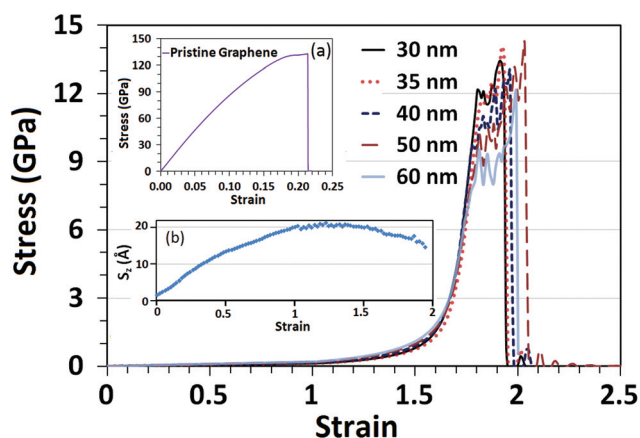
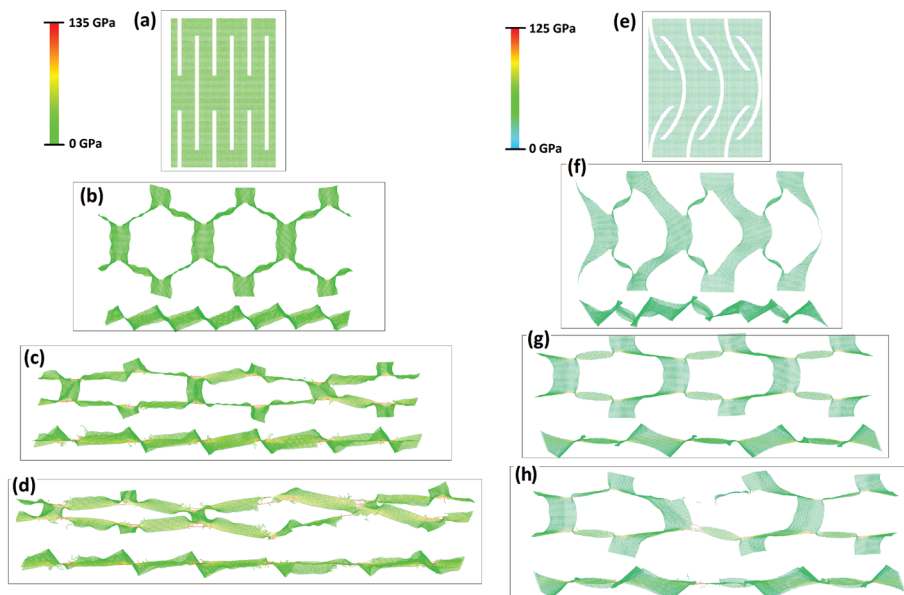


Fig. 5 Stress–strain responses of the graphene kirigami structures with linear cuts and with different lengths (ranging from 30 nm to 60 nm). The inset (a) illustrates the stress–strain relation of pristine graphene. The inset (b) shows the computed standard deviation of the  $z$ -coordinates ( $S_z$ ) for a graphene kirigami with a cut length of 40 nm.



**Fig. 6** Top and side views of the deformation process and stress distribution (in GPa) of graphene kirigami with periodic (a–d) linear and (e–h) 90 degree, 40 nm long cuts. The strain levels for different snapshots are as follows: (a and e) 0.0, (b) 1.2, (c) 1.6, (d) 1.8, (f) 1.0, (g) 1.45 and (h) 1.6. The OVITO package<sup>71</sup> has been used to illustrate these deformed structures.

metrical which verifies the accuracy of our applied loading condition and also confirms that our modeling results are representative of graphene kirigami structures with a periodic pattern of cuts. Moreover, up to high strain levels the stretching is achieved by the out-of plane deflections of the sheets and transverse shrinkage and the stress values throughout the sample are negligible, though in the cut corners due to stress concentration they may instantaneously reach high values (Fig. 6(b) and (f)). At the higher strain levels around the failure, the stress concentration increases around the cut corners which initiate spontaneous bond breakage (Fig. 6(b) and (f)), finally leading to sample rupture (Fig. 6(d) and (h)). As is clear, to design highly stretchable graphene kirigami, the solution is to enhance the deflection limit of the structures. In this regard, linear cuts are more favorable since they can deflect more than curved cuts. In addition, a simple comparison based on Fig. 6 results reveals that upon the stretching, the kirigami structure with linear cuts shrinks more along the transverse direction in comparison with the curved cuts.

To provide a general viewpoint concerning the engineering of the graphene kirigami mechanical response, we studied the effects of various design parameters. To this aim, we compared the rupture strain and tensile strength for different kirigami structures. The rupture strain is the key parameter which is representative of the stretchability of the graphene nanomembranes. The stress field in linear elastic fracture mechanics (LEFM)<sup>72</sup> in a two dimensional solid for a straight crack can be described in terms of mode I (opening mode by tensile stress) and II (sliding mode caused by shear stress) stress intensity factors. We should however emphasise that although our study is categorized as a large deformation problem, the insight pro-

vided by the LEFM for small strain theory can be helpful in understanding the underlying mechanism. The stress intensity factor for the arrangement of cracks in the transverse direction can be computed using the standard fracture mechanics techniques, as follows:<sup>72</sup>

$$K_I = \sigma_\infty \sqrt{(2h) \tan\left(\frac{\pi a}{2h}\right)} \quad (3)$$

Here  $a$  is the cut length,  $h$  is the sum of the cut length and transverse spacing distance, and  $\sigma_\infty$  is the applied uniform stress. As shown in Fig. 7(a), by increasing the transverse spacing ratio, both the rupture strain and the tensile strength increase. The increase in the maximum tensile strength is more considerable than the increase in the stretchability. The value of the stress near the cut tip decreases with increasing the transverse distance. Therefore, the larger the transverse spacing between the cracks, the less is the influence from the interaction of the near tip stress fields. According to eqn (3), the stress-intensity factor decreases by increasing the transverse spacing distance due to the suppression of the interaction of the stress fields of adjacent cuts. Consequently, by increasing the transverse spacing ratio, the stress-concentration decreases such that the tensile strength increases. Note that for a very high transverse spacing the graphene kirigami approaches the graphene structure with few cracks inside, which yields a failure strain lower than that of the pristine graphene. For the graphene kirigami accordingly there should be an optimum transverse spacing distance that maximizes the stretchability. The situation is opposite for the increase of the longitudinal spacing ratio. Indeed, by increasing the longitudi-

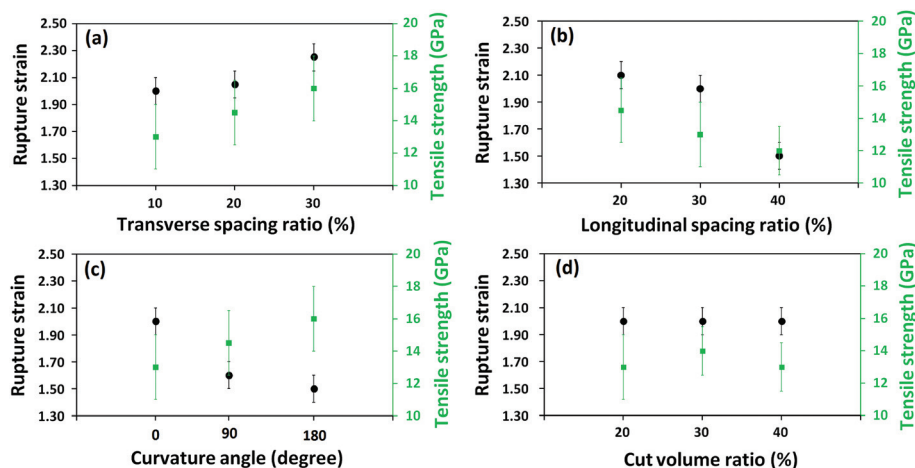


Fig. 7 Effect of various design parameters such as (a) the transverse and (b) longitudinal spacing ratio, (c) curvature angle and (d) cut volume ratio on the rupture strain (stretchability) and tensile strength of graphene kirigami structures.

nal spacing, the stretchability decreases significantly. This is an expected trend because the stretchability of the kirigami structures is basically originated from the longitudinal spacing. By increasing the longitudinal spacing, the out-of-plane deflection decreases and the structure approaches that of the graphene film with cracks.

Regarding the cut curvature angle, we found that the linear cuts present the highest stretchability as shown in Fig. 7(c). For the linear cuts, the rupture strain is higher than the one for curved cracks due to the fact that the effective distance between two curved cuts becomes much smaller. Hence, for the curved cuts, the film deflection decreases and additionally the crack path until coalescence is shorter and therefore the stretchability is not as high as for the linear cuts. Nonetheless, it has been shown by Karihaloo<sup>73</sup> that the stress intensity factor for a curved crack is lower compared to that of the straight crack of the same length being positioned at the same location and subjected to far field stress. Therefore, by increasing the cut curvature angle, the stress concentration decreases such that the tensile strength increases. Interestingly, for the cut volume fraction, we found that it does not yield considerable effects either on the stretchability or on the tensile strength (see Fig. 7(d)). Based on our brief parametric investigation, the transverse and longitudinal spacing ratios can be considered as the two main factors that could be optimized to increase both stretchability and tensile strength. Our results also clearly confirm that the graphene kirigami structures can be stretchable by more than 10 times as compared with pristine graphene.

### C. Electronic structures

After having explored their thermal and mechanical properties, we now focus on the electronic structure properties of the graphene kirigami. First, the density of states (DOS) of various graphene kirigami structures are shown in Fig. 8. The total widths/lengths of the large systems vary between 320 and 390 nm and

are obtained by repeating the unit cells as shown in Fig. 8 (left panels). The total size of the system is large enough to ensure an accurate energy resolution within the Lanczos technique and also a rapid convergence of the average on random phase wave packets. Note that three different angles were considered for the cuts,  $\theta_c = 0, 90$ , and  $180^\circ$ . For  $\theta_c = 0^\circ$ , the cuts are actually straight (Fig. 8(a–d)), while for  $90$  and  $180^\circ$ , the cuts are curved (Fig. 8(f–i, k–n)). For each  $\theta_c$ , five different cut lengths are considered,  $l_c = 10, 20, 40, 80$ , and  $160$  nm (the unit cells of the  $l_c = 160$  nm systems are not shown in Fig. 8).

The DOS of the case  $\theta_c = 0^\circ$  for different cut lengths  $l_c$  are shown in Fig. 8(e), while the DOS corresponding to  $\theta_c = 90$  and  $180^\circ$  are shown in Fig. 8(j) and (o), respectively. One recognizes easily the global shape of the graphene DOS corresponding to the  $\pi$  and  $\pi^*$  bands, *i.e.* a Heaviside function at the band edges ( $\Gamma$  point in the graphene Brillouin zone (BZ)), two van Hove singularities ( $M$  point in the BZ), and a V-shape, *i.e.* a linear increase as a function of energy around the Dirac point ( $K$  point in the BZ). However, one also obviously notices the presence of many DOS sub-peaks which can be attributed to van Hove singularities typical of 1D systems, which appear because of the formation of connected nanoribbons generated by the cuts in graphene. The energy spacing between these 1D van Hove singularities is inversely proportional to the ribbon's width. For very thin ribbons ( $l_c = 10$  nm cases, see for instance Fig. 8(a)), the DOS is quite spiky and deviates considerably from the pristine graphene DOS, in particular close to the Fermi energy (Dirac point in graphene) where the DOS substructure is complex (see the insets in Fig. 8(e, j and o)). In particular, small energy gaps can appear as observed, for instance, for  $(\theta_c, l_c) = (90^\circ, 10$  nm) and  $(180^\circ, 10$  nm), while a more significant gap is observed for  $(\theta_c, l_c) = (0^\circ, 20$  nm) in the energy range  $[-0.2, +0.2]$  eV with a peak centered on the zero energy. However, when increasing  $l_c$  the DOS recovers progressively the shape of pristine graphene DOS although residual oscillations coming from the 1D van Hove singularities are still

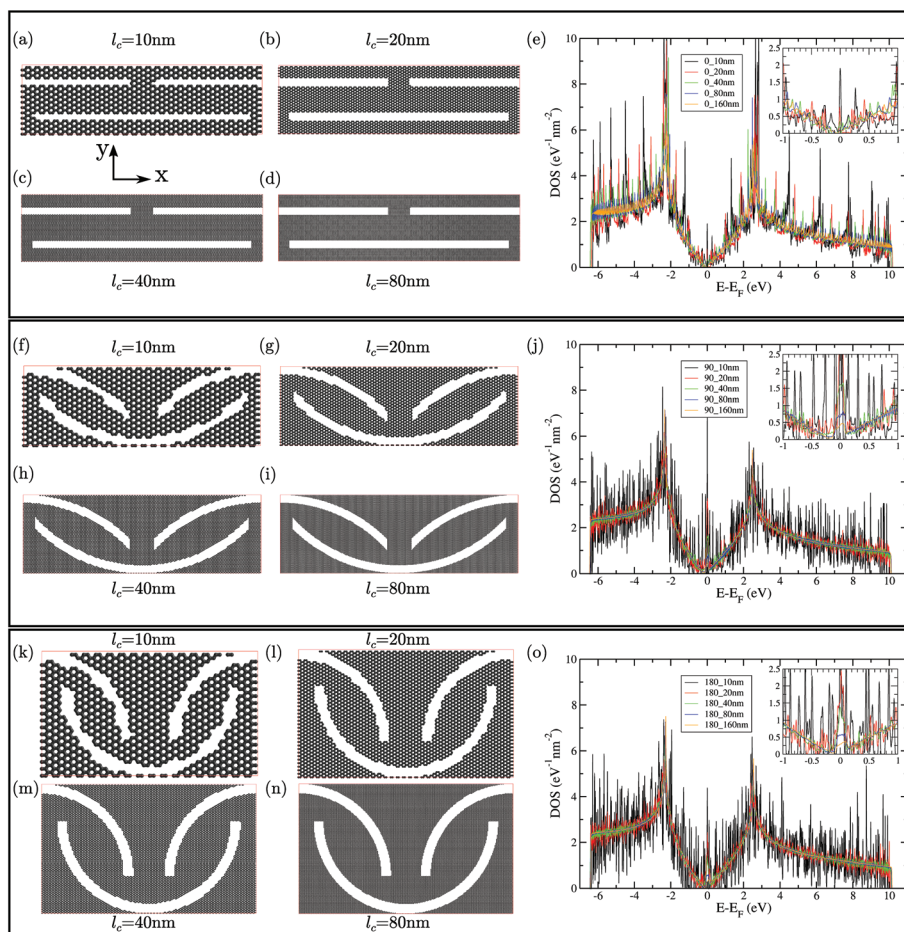


**Fig. 8** Atomic structures of graphene kirigami obtained with various cut angles ( $\theta_c$ ) and cut lengths ( $l_c$ ) and their associated DOS. Top panels (a–e): Unit cells of graphene kirigami corresponding to  $\theta_c = 0^\circ$  and  $l_c = 10, 20, 40,$  and  $80$  nm (a, b, c and d), respectively, and the associated DOS (e). Middle panels (f–j): Unit cells of graphene kirigami corresponding to  $\theta_c = 90^\circ$  and  $l_c = 10, 20, 40,$  and  $80$  nm (f, g, h and i), respectively, and the associated DOS (j). Bottom panels (k–o): Unit cells of graphene kirigami corresponding to  $\theta_c = 180^\circ$  and  $l_c = 10, 20, 40,$  and  $80$  nm (k, l, m and n), respectively, and the associated DOS (o).

present. Note that for  $\theta_c = 90$  and  $180^\circ$ , although the DOS become similar to graphene DOS, a non-negligible peak remains present around the Fermi energy (see for instance  $l_c = 80, 160$  nm curves in the insets of Fig. 8(j and o)). These persistent peaks are originating from strongly localized states, most probably located close to the cut edges, similar to what was observed for vacancies in graphene.<sup>74</sup> Such localized states can affect the electronic transport and can possibly induce a transport gap in the corresponding energy window.

#### D. Electronic transport

Recently, Bahamon *et al.* discussed the electronic transport in 34 nm long and 10 nm wide 1D graphene kirigami structures with straight cuts using the Landauer–Büttiker formalism.<sup>75</sup> They observed that at this nanoscale size the 1D electronic transport is governed by resonant tunneling through coupled localized states acting as quantum dots. Upon moderate elongation (15%), the conductance profile is first degraded because of the decoupling of the states but it can revive at a

larger elongation (30%). Similar to graphene kirigami structures, graphene nanomeshes and antidot lattices can also be highly stretchable in certain circumstances.<sup>76</sup> Electronic and thermal transport in such graphene nanomeshes have been intensively studied, showing interesting thermoelectric properties.<sup>77–80</sup>

Here, the electronic transport properties of unstretched 2D periodic graphene kirigami are investigated using the real-space Kubo–Greenwood method. As discussed in the Models and method section, the Kubo–Greenwood formalism allow us to describe the electronic diffusion and the associated conductivity. The diffusivity curves are shown in the ESI.† They illustrate the discussion conducted in the Models and method section regarding the presence of the two-scale periodicity and its impact on the ballistic and intermediate diffusive/localized transport regimes. However, in order to gain more insight and obtain a more concrete picture of the electronic transport properties in these systems, it is preferable to characterize them through the energy- and length-dependent Kubo–Greenwood

conductivity  $\sigma(E,L)$ . The longitudinal components of the conductivity tensor  $\sigma_{xx}(E,L)$  and  $\sigma_{yy}(E,L)$  have been calculated for three specific propagation lengths  $L = 20, 60$  and  $100$  nm and are shown in Fig. 9. One can immediately notice three points. First, it is clear that the conductivities along the Y direction (gray, orange and cyan curves) are much lower than the conductivities along the X direction (black, red and blue curves). Second, the increase of the cut angle from  $\theta_c = 0^\circ$  to  $\theta_c = 180^\circ$  (*i.e.* from left to right panels) decreases the overall conductivity profile in absolute values. Finally, the transition from a 1D nanoribbon-like to a 2D graphene-like electronic transport is

clearly visible when going from small to large cut lengths  $l_c$  (*i.e.* from top to bottom panels) as the 1D subband structure is progressively smoothed out. The conductivities  $\sigma_{xx}(E,L)$  and  $\sigma_{yy}(E,L)$  are found to globally increase with the propagation length although the increase is not really significant for  $\sigma_{yy}(E,L)$  which is maintained to low values. Actually, for high cut angle and long cut lengths,  $\sigma_{yy}(E,L)$  displays a decreasing behavior synonym of localization effects. Note also that for  $\sigma_{yy}$  the propagation length  $L = 100$  nm is not reached at all energies  $E$  because of the slow propagation velocities in this direction. As for thermal transport, these results demonstrate a

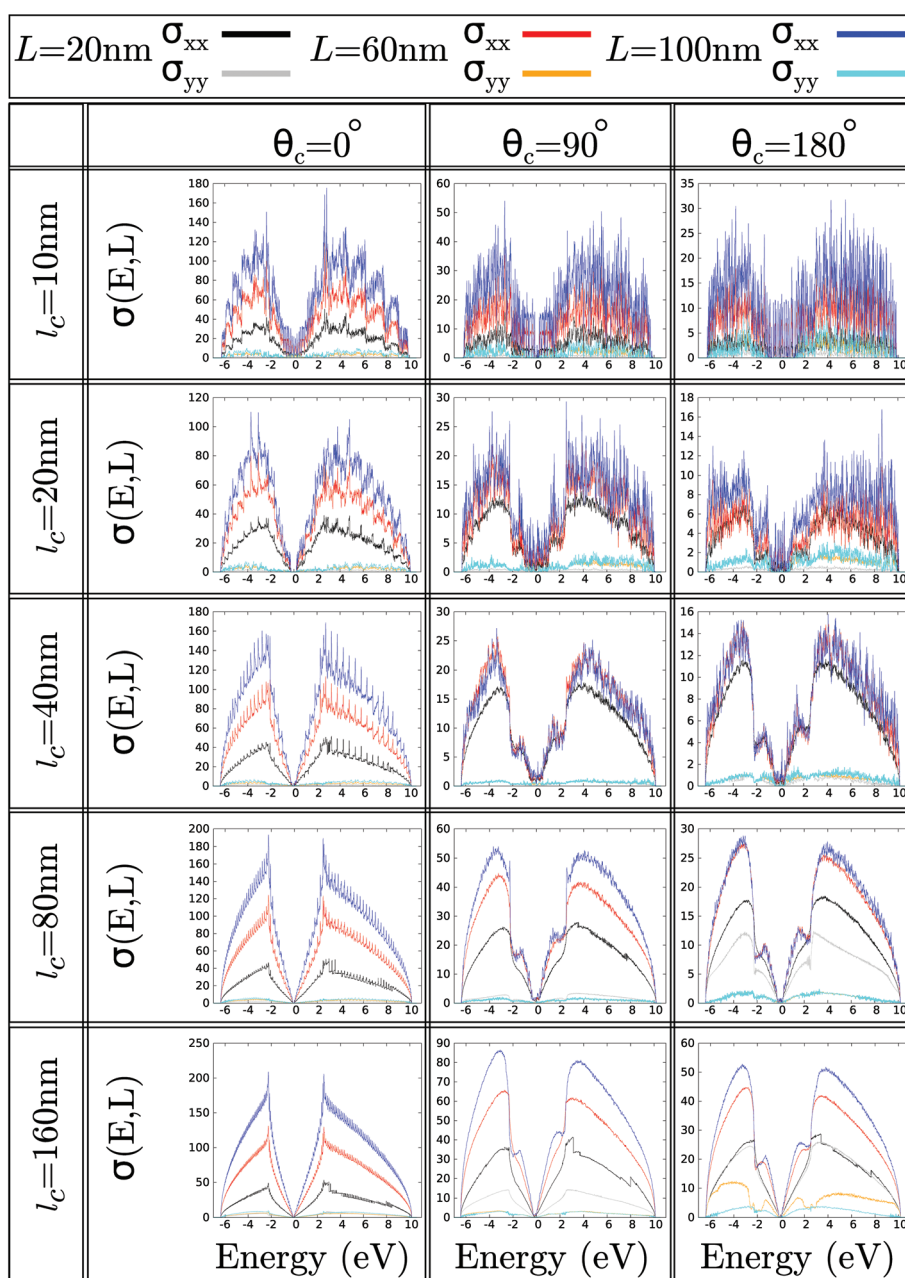


Fig. 9 Electronic conductivity ( $\sigma(E,L)$ ) in units of  $G_0 = 2e^2/h$  for various kirigami structures with (from left to right) cut angles  $\theta_c = 0, 90$ , and  $180^\circ$ , and (from top to bottom) cut lengths  $l_c = 10, 20, 40, 80$ , and  $160$  nm.

strong anisotropy between the two principal electronic transport directions. Then, as noticed in the DOS, the presence of a bandgap is clearly observed in the system  $(\theta_c, l_c) = (0^\circ, 20 \text{ nm})$ . Interestingly, the general shape of  $\sigma_{xx}$  for curved cuts is different from the  $\theta_c = 0^\circ$  case. Indeed, the electron/hole regions (positive/negative charge carrier energies) exhibit two main peaks instead of only one. There are no particular features in the DOS that would help to explain this double peak structure. Actually, it is interesting to note that for  $(\theta_c, l_c) = (180^\circ, 160 \text{ nm})$  the conductivity curve exhibits a single peak structure at small propagation length ( $L = 20 \text{ nm}$ ) before showing a double peak structure at longer propagation length ( $L = 100 \text{ nm}$ ). Overall, a conductivity ratio  $\frac{\sigma_{xx}}{\sigma_{yy}} \sim 10 - 20$  can be estimated.

## IV. Concluding remarks

Extensive atomistic simulations were conducted to explore the electronic and thermal transport as well as the stretchability of graphene kirigami structures. The properties of graphene kirigami structures were investigated using periodic patterns of linear and curved cuts. The equilibrium molecular dynamics (EMD) method was used to calculate the effective thermal conductivity of graphene kirigami structures at the atomic scale. The thermal transport is found to be highly anisotropic and the phonon-cut scattering effect plays the major role in the heat transport. The effective thermal conductivity of graphene kirigami structures as a function of cut lengths was established by extrapolating the EMD results for small cut lengths to the estimation based on the finite element (FE) diffusive modeling. It was confirmed that the proposed combination of EMD and FE modeling can be accurately used to evaluate the effective thermal conductivity of graphene kirigami structures from the nano- to the macroscale. Notably, our results suggest that the thermal conductivity of graphene can be engineered by more than three orders of magnitude based on the kirigami approach. Then, the mechanical responses of graphene kirigami structures were investigated by performing uniaxial tensile molecular dynamics simulations. Up to high strain levels, the kirigami structure elongates by out-of-plane deflection rather than bond stretching and thus the stress values remain negligible. The stress values later start to increase smoothly, implying that bond elongation also occurs. Before the failure point, the stress values increase sharply and the existing stress concentrations around the cut corners result in bond breakages and finally lead to the sample rupture. Consequently, the stretchability of the graphene kirigami was suggested to directly correlate to the out-of-plane deflection limit of the structure which can be improved by using the straight cuts with optimized transverse and longitudinal spacing ratios. Finally, electronic transport was investigated. The electronic density of states displayed a series of van Hove peaks which are the signature of a one-dimensional confinement in the case of graphene kirigami at the nanoscale.

Bandgaps can even occur in some cases, as well as transport gaps caused by strongly localized states especially in curved cuts. Finally, electronic conductivities are found to be highly anisotropic with a ratio of  $\sim 10-20$ . Unfortunately, this electronic anisotropy is analogous to the thermal anisotropy which is in principle not in favor of thermoelectric applications. However, as discussed, the tunability of graphene kirigami properties is very large and therefore may open routes towards thermoelectric engineering and new kinds of ultra-thin NEMS with superior properties.

## Conflicts of interest

There are no conflicts of interest to declare.

## Acknowledgements

B. M. and T. R. greatly acknowledge the financial support by the European Research Council for COMBAT project (Grant number 615132). Z. F. and A. H. are supported by the National Natural Science Foundation of China (Grant No. 11404033) and the Academy of Finland through its Centres of Excellence Program (project no. 251748) and they acknowledge the computational resources provided by the Aalto Science-IT project and Finland's IT Center for Science (CSC). A. L., and J.-C. C. acknowledge financial support from the Fédération Wallonie-Bruxelles through the ARC entitled 3D Nanoarchitecturing of 2D crystals (no. 16/21-077), from the European Union's Horizon 2020 research and innovation programme (no. 696656), and from the Belgium FNRS. Computational resources have been partly provided by the supercomputing facilities of the Université catholique de Louvain (CISM/UCL) and the Consortium des Équipements de Calcul Intensif en Fédération Wallonie Bruxelles (CÉCI) funded by the Fond de la Recherche Scientifique de Belgique (F.R.S.-FNRS) under convention 2.5020.11.

## References

- 1 K. S. Novoselov, A. K. Geim, S. V. Morozov, D. Jiang, Y. Zhang, S. V. Dubonos, I. V. Grigorieva and A. A. Firsov, *Science*, 2004, **306**, 666.
- 2 A. K. Geim and K. S. Novoselov, *Nat. Mater.*, 2007, **6**, 183.
- 3 A. H. Castro Neto, F. Guinea, N. M. R. Peres, K. S. Novoselov and A. K. Geim, *Rev. Mod. Phys.*, 2009, **81**, 109.
- 4 C. Lee, X. Wei, J. W. Kysar and J. Hone, *Science*, 2008, **321**, 385.
- 5 A. A. Balandin, *Nat. Mater.*, 2011, **10**, 569.
- 6 S. Ghosh, W. Bao, D. L. Nika, S. Subrina, E. P. Pokatilov, C. N. Lau and A. A. Balandin, *Nat. Mater.*, 2010, **9**, 555.
- 7 Y. Kubota, K. Watanabe, O. Tsuda and T. Taniguchi, *Science*, 2007, **317**, 932.
- 8 B. Aufray, A. Kara, S. Vizzini, H. Oughaddou, C. Léandri, B. Ealet and G. L. Lay, *Appl. Phys. Lett.*, 2010, **96**, 183102.

- 9 P. Vogt, P. De Padova, C. Quaresima, J. Avila, E. Frantzeskakis, M. C. Asensio, A. Resta, B. Ealet and G. Le Lay, *Phys. Rev. Lett.*, 2012, **108**, 155501.
- 10 S. Das, M. Demarteau and A. Roelofs, *ACS Nano*, 2014, **8**, 11730.
- 11 L. Li, Y. Yu, G. J. Ye, Q. Ge, X. Ou, H. Wu, D. Feng, X. H. Chen and Y. Zhang, *Nat. Nanotechnol.*, 2014, **9**, 372.
- 12 A. J. Mannix, X.-F. Zhou, B. Kiraly, J. D. Wood, D. Alducin, B. D. Myers, X. Liu, B. L. Fisher, U. Santiago, J. R. Guest, M. J. Yacaman, A. Ponce, A. R. Oganov, M. C. Hersam and N. P. Guisinger, *Science*, 2015, **350**, 1513.
- 13 E. Bianco, S. Butler, S. Jiang, O. D. Restrepo, W. Windl and J. E. Goldberger, *ACS Nano*, 2013, **7**, 4414.
- 14 B. Radisavljevic, A. Radenovic, J. Brivio, V. Giacometti and A. Kis, *Nat. Nanotechnol.*, 2011, **6**, 147.
- 15 J. Chen, J. H. Walther and P. Koumoutsakos, *Adv. Funct. Mater.*, 2015, **25**, 7539.
- 16 S. Hu, J. Chen, N. Yang and B. Li, *Carbon*, 2017, **116**, 139.
- 17 Z. Zhang, S. Hu, J. Chen and B. Li, *Nanotechnology*, 2017, **28**, 225704.
- 18 F. Guinea, *Solid State Commun.*, 2012, **152**, 1437.
- 19 C. Metzger, S. Rémi, M. Liu, S. V. Kusminskiy, A. H. Castro Neto, A. K. Swan and B. B. Goldberg, *Nano Lett.*, 2010, **10**, 6.
- 20 V. M. Pereira and A. H. Castro Neto, *Phys. Rev. Lett.*, 2009, **103**, 046801.
- 21 S. Barraza-Lopez, A. A. P. Sanjuan, Z. Wang and M. Vanević, *Solid State Commun.*, 2013, **166**, 70.
- 22 F. Guinea, M. I. Katsnelson and A. K. Geim, *Nat. Phys.*, 2010, **6**, 30.
- 23 F. Banhart, J. Kotakoski and A. V. Krasheninnikov, *ACS Nano*, 2011, **5**, 26.
- 24 A. Lherbier, S. M.-M. Dubois, X. Declerck, Y.-M. Niquet, S. Roche and J.-C. Charlier, *Phys. Rev. B: Condens. Matter*, 2012, **86**, 075402.
- 25 A. W. Cummings, D. L. Duong, V. L. Nguyen, D. Van Tuan, J. Kotakoski, J. E. Barrios Vargas, Y. H. Lee and S. Roche, *Adv. Mater.*, 2014, **26**, 5079.
- 26 A. Cresti, N. Nemeč, B. Biel, G. Niebler, F. Triozon, G. Cuniberti and S. Roche, *Nano Res.*, 2008, **1**, 361.
- 27 T. O. Wehling, K. S. Novoselov, S. V. Morozov, E. E. Vdovin, M. I. Katsnelson, A. K. Geim and A. I. Lichtenstein, *Nano Lett.*, 2008, **8**, 173.
- 28 A. Lherbier, X. Blase, Y.-M. Niquet, F. M. C. Triozon and S. Roche, *Phys. Rev. Lett.*, 2008, **101**, 036808.
- 29 X. Wang, L. Zhi and K. Millen, *Nano Lett.*, 2008, **8**, 323.
- 30 F. Schedin, A. K. Geim, S. V. Morozov, E. W. Hill, P. Blake, M. I. Katsnelson and K. S. Novoselov, *Nat. Mater.*, 2007, **6**, 652.
- 31 X. Miao, S. Tongay, M. K. Petterson, K. Berke, A. G. Rinzler, B. R. Appleton and A. F. Hebard, *Nano Lett.*, 2012, **12**, 2745.
- 32 D. Soriano, D. V. Tuan, S. M.-M. Dubois, M. Gmitra, A. W. Cummings, D. Kochan, F. Ortmann, J.-C. Charlier, J. Fabian and S. Roche, *2D Mater.*, 2015, **2**, 022002.
- 33 P. Zhang, L. Ma, F. Fan, Z. Zeng, C. Peng, P. E. Loya, Z. Liu, Y. Gong, J. Zhang, X. Zhang, P. M. Ajayan, T. Zhu and J. Lou, *Nat. Commun.*, 2014, **5**, 3782.
- 34 M. K. Blees, A. W. Barnard, P. A. Rose, S. P. Roberts, K. L. McGill, P. Y. Huang, A. R. Ruyack, J. W. Kevek, B. Kobrin, D. A. Muller and P. L. McEuen, *Nature*, 2015, **524**, 204.
- 35 J. Feng, W. Li, X. Qian, J. Qi, L. Qi and J. Li, *Nanoscale*, 2012, **4**, 4883.
- 36 Z. Qi, D. K. Campbell and H. S. Park, *Phys. Rev. B: Condens. Matter*, 2014, **90**, 245437.
- 37 P. Z. Hanakata, Z. Qi, D. K. Campbell and H. S. Park, *Nanoscale*, 2016, **8**, 458.
- 38 N. Wei, Y. Chen, K. Cai, J. Zhao, H.-Q. Wang and J.-C. Zheng, *Carbon*, 2016, **104**, 203.
- 39 T. C. Shyu, P. F. Damasceno, P. M. Dodd, A. Lamoureux, L. Xu, M. Shlian, M. Shtein, S. C. Glotzer and N. A. Kotov, *Nat. Mater.*, 2015, **14**, 785.
- 40 J. Tersoff, *Phys. Rev. B: Condens. Matter*, 1988, **37**, 6991.
- 41 J. Tersoff, *Phys. Rev. Lett.*, 1988, **61**, 2879.
- 42 L. Lindsay and D. A. Broido, *Phys. Rev. B: Condens. Matter*, 2010, **81**, 205441.
- 43 X. Xu, L. F. C. Pereira, Y. Wang, J. Wu, K. Zhang, X. Zhao, S. Bae, C. Tinh Bui, R. Xie, J. T. L. Thong, B. H. Hong, K. P. Loh, D. Donadio, B. Li and B. Özyilmaz, *Nat. Commun.*, 2014, **5**, 3689.
- 44 B. Mortazavi, Z. Fan, L. F. C. Pereira, A. Harju and T. Rabczuk, *Carbon*, 2016, **103**, 318.
- 45 Z. Fan, L. F. C. Pereira, H.-Q. Wang, J.-C. Zheng, D. Donadio and A. Harju, *Phys. Rev. B: Condens. Matter*, 2015, **92**, 094301.
- 46 Z. Fan, W. Chen, V. Vierimaa and A. Harju, *Comput. Phys. Commun.*, 2017, **218**, 10.
- 47 P. K. Schelling, S. R. Phillpot and P. Keblinski, *Phys. Rev. B: Condens. Matter*, 2002, **65**, 144306.
- 48 S. Plimpton, *J. Comput. Phys.*, 1995, **117**, 1.
- 49 D. Mayou and S. N. Khanna, *J. Phys. I France*, 1995, **5**, 1199.
- 50 F. Triozon, J. Vidal, R. Mosseri and D. Mayou, *Phys. Rev. B: Condens. Matter*, 2002, **65**, 220202.
- 51 S. Latil, S. Roche, D. Mayou and J.-C. Charlier, *Phys. Rev. Lett.*, 2004, **92**, 256805.
- 52 Y.-M. Niquet, A. Lherbier, M. P. Persson, F. Triozon, S. Roche, X. Blase and D. Rideau, 13th International Workshop on Computational Electronics, IWCE, 2009, IEEE Xplore, pp. 1–4.
- 53 N. Leconte, A. Lherbier, F. Varchon, P. Ordejón, S. Roche and J.-C. Charlier, *Phys. Rev. B: Condens. Matter*, 2011, **84**, 235420.
- 54 A. Uppstu, Z. Fan and A. Harju, *Phys. Rev. B: Condens. Matter*, 2014, **89**, 075420.
- 55 J.-J. Adjizian, A. Lherbier, S. M.-M. Dubois, A. R. Botello-Mendez and J.-C. Charlier, *Nanoscale*, 2016, **8**, 1642.
- 56 V. M. Pereira, A. H. Castro Neto and N. M. R. Peres, *Phys. Rev. B: Condens. Matter*, 2009, **80**, 045401.
- 57 A. Lherbier, S. Roche, O. A. Restrepo, Y.-M. Niquet, A. Delcorte and J.-C. Charlier, *Nano Res.*, 2013, **6**, 326.
- 58 R. Haydock, *Comput. Phys. Commun.*, 1980, **20**, 11.
- 59 H. Khalfoun, A. Lherbier, P. Lambin, L. Henrard and J.-C. Charlier, *Phys. Rev. B: Condens. Matter*, 2015, **91**, 035428.

- 60 E. Lampin, P. L. Palla, P.-A. Francioso and F. Cleri, *J. Appl. Phys.*, 2013, **114**, 033525.
- 61 Z. Fan, L. F. C. Pereira, P. Hirvonen, M. M. Ervasti, K. R. Elder, D. Donadio, T. Ala-Nissila and A. Harju, *Phys. Rev. B: Condens. Matter*, 2017, **95**, 144309.
- 62 G. Barbarino, C. Melis and L. Colombo, *Phys. Rev. B: Condens. Matter*, 2015, **91**, 035416.
- 63 J. Chen, G. Zhang and B. Li, *Nanoscale*, 2013, **5**, 532.
- 64 B. Mortazavi, M. Potschke and G. Cuniberti, *Nanoscale*, 2014, **6**, 3344.
- 65 B. Mortazavi and S. Ahzi, *Solid State Commun.*, 2012, **152**, 1503.
- 66 A.-X. Zhang, J.-T. Liu, S.-D. Guo and H.-C. Li, *Phys. Chem. Chem. Phys.*, 2017, **19**, 14520.
- 67 H. Xie, T. Ouyang, E. Germaneau, G. Qin, M. Hu and H. Bao, *Phys. Rev. B: Condens. Matter*, 2016, **93**, 075404.
- 68 Y. D. Kuang, L. Lindsay, S. Q. Shi and G. P. Zheng, *Nanoscale*, 2016, **8**, 3760.
- 69 B. Mortazavi, M.-Q. Le, T. Rabczuk and L. F. C. Pereira, *Physica E*, 2017, **93**, 202.
- 70 J. Chen, J. H. Walther and P. Koumoutsakos, *Nano Lett.*, 2014, **14**, 819.
- 71 A. Stukowski, *Modell. Simul. Mater. Sci. Eng.*, 2010, **18**, 015012.
- 72 K. B. Broberg, *Cracks and Fracture*, Academic Press, 1999.
- 73 B. Karihaloo, *Mech. Mater.*, 1982, **1**, 189.
- 74 A. Cresti, T. Louvet, F. Ortmann, D. Van Tuan, P. Lenarczyk, G. Huhs and S. Roche, *Crystals*, 2013, **3**, 289.
- 75 D. A. Bahamon, Z. Qi, H. S. Park, V. M. Pereira and D. K. Campbell, *Phys. Rev. B: Condens. Matter*, 2016, **93**, 235408.
- 76 S. Zhu, Y. Huang and T. Li, *Appl. Phys. Lett.*, 2014, **104**, 173103.
- 77 T. Gunst, T. Markussen, A.-P. Jauho and M. Brandbyge, *Phys. Rev. B: Condens. Matter*, 2011, **84**, 155449.
- 78 H. Karamitaheri, M. Pourfath, M. Pazoki, R. Faez and H. Kosina, *J. Electrochem. Soc.*, 2011, **158**, K213.
- 79 H. Karamitaheri, M. Pourfath, R. Faez and H. Kosina, *J. Appl. Phys.*, 2011, **110**, 054506.
- 80 J. Oh, H. Yoo, J. Choi, J. Y. Kim, D. S. Lee, M. J. Kim, J.-C. Lee, W. N. Kim, J. C. Grossman, J. H. Park, S.-S. Lee, H. Kim and J. G. Son, *Nano Energy*, 2017, **35**, 26.